RESEARCH ARTICLE | DECEMBER 09 2024

Interfacial vs confinement effects in the anisotropic frequency-dependent dielectric, THz and IR response of nanoconfined water

Maximilian R. Becker ; Roland R. Netz

J. Chem. Phys. 161, 224704 (2024)
https://doi.org/10.1063/5.0239693

The Journal of Chemical Physics ARTICLE pubs.aip.org/aip/jcp

Interfacial vs confinement effects in the anisotropic frequency-dependent dielectric, THz and IR response of nanoconfined water

Cite as: J. Chem. Phys. 161, 224704 (2024); doi: 10.1063/5.0239693
Submitted: 21 September 2024 • Accepted: 14 November 2024 •
Published Online: 9 December 2024

Maximilian R. Becker and Roland R. Netz[a)]

AFFILIATIONS

Fachbereich Physik, Freie Universität Berlin, 14195 Berlin, Germany

[a)]Author to whom correspondence should be addressed: rnetz@physik.fu-berlin.de

ABSTRACT

We investigate the anisotropic frequency-dependent dielectric, THz and IR response of liquid water confined between two planar graphene sheets with force-field- and density-functional-theory-based molecular dynamics simulations. Using spatially resolved anisotropic spectra, we demonstrate the critical role of the volume over which the spectral response is integrated when reporting spatially averaged electric susceptibilities. To analyze the spectra, we introduce a unique decomposition into bulk, interfacial, and confinement contributions, which reveals that confinement effects on the spectra occur only for systems with graphene separation below 1.4 nm, for all frequencies. Based on this decomposition, we discuss the molecular origin of the main absorption features of nanoconfined water from the GHz to the IR regime. We show that, at low frequencies, the 15 GHz Debye peak of interfacial water is redshifted due to a slowdown of collective water reorientations. At high frequencies, the OH stretch at 100 THz blue shifts and a signature of free OH groups emerges, while the HOH bend mode at 50 THz is redshifted. Strikingly, in nanoconfinement, the 20 THz libration band shifts to below 15 THz and broadens drastically, spanning two orders of magnitude in frequency. These results are rationalized by the collective water motion and the structure of the hydrogen-bond network at the water–graphene interface and in two-dimensional water layers, which reveals the intricate behavior of nanoconfined water and its spectral properties.

I. INTRODUCTION

The alteration of structural and dynamical properties of liquid water in nanoconfinement has been the subject of extensive theoretical and experimental research due to its far-reaching implications in material sciences, chemistry, and biology.[1–5] The frequency-dependent electric response provides a fingerprint of these properties over multiple time scales. Based on different spectroscopic techniques, such as linear infrared (IR) spectroscopy,[6–9] time-resolved Kerr effect spectroscopy,[10,11] and pump–probe spectroscopy,[12–14] significant alterations of hydrogen-bond patterns and reorientation dynamics have been observed in confined geometries. Various studies have detected a confinement-induced blue shift of the OH stretch peak at 100 THz.[6,7,12,15] By decomposing the OH stretch feature into three different hydrogen-bond populations, this has been argued to be linked to a decrease in connectivity of the hydrogen-bond network in the vicinity of interfaces.[6,7] The hydrogen-bond network has also been analyzed based on the hydrogen-bond stretch peak at around 5 THz[7,16] showing a blue shift and decrease in linewidth with respect to bulk, whose origin remains under debate. Finally, by analyzing spectral diffusion and anisotropic decay from 2D IR spectroscopy experiments, a rotational slowdown of water molecules in confinement has been found,[13,17] similar to what has been described in the hydration shell of hydrophobic solutes.[18,19]

In order to assign observed spectral changes to either surface or finite-size (confinement) effects, systematic studies at varying confinement lengths are typically performed. For spectroscopic techniques that are not surface sensitive, the results are then interpreted in terms of a "core–shell" or "two-state" model,[20,21] which assigns different properties to water molecules in the vicinity of interfaces and in bulk. Depending on assumptions made about the total water

content of the measured systems, interfacial layer widths of a few Å have been obtained, in line with molecular dynamics (MD) simulations, which show that liquid properties deviate from bulk behavior in interfacial layers with a thickness of only a few Å.[22–24] However, there is an ongoing discussion about the maximum confinement length below which the interfacial layers start interacting with each other and the core–shell model loses its validity. Some experimental studies argue confinement effects to be relevant for confinement lengths as large as 100 nm.[7,15,25] Recently, surface-sensitive sum-frequency generation spectroscopy determined the confinement size below which confinement effects become relevant as being smaller than a nanometer.[26]

In recent years, MD simulations have been widely used to study water in nanoconfinement, as they can spatially resolve kinetic molecular properties such as diffusional, vibrational, or reorientational dynamics in confinement,[27–33] reproducing and explaining the aforementioned experimental results. Most prominently, the apparent dependence of the static dielectric constant of water confined between planar graphene sheets[34] on confinement length was explained in terms of a dielectric surface layer,[35–39] whose thickness is largely independent of graphene sheet separation. In this context, a dielectric dividing surface[22] has been introduced, whose distance to the Gibbs dividing surface quantifies the dielectric excess of a general solid–liquid interface. For systems with confinement length smaller than 1.5 nm, the position of the dielectric dividing surface has been shown to deviate from its large-system value for various solid–water systems, indicating the emergence of confinement effects.[29,36,37,40] However, a general scheme to quantify frequency-dependent confinement effects is still lacking. This work aims at bridging this gap.

In this work, we calculate spatially resolved and frequency-dependent electric susceptibilities of water in planar nanoconfinement. We introduce a box model, which yields effective spectra that can be compared to spatially averaged spectra from typical experimental measurements. Our model reveals a very strong sensitivity of the spatially averaged susceptibility to the integration volume. We further propose a decomposition scheme, independent of the definition of an interfacial water layer and applicable to experimental data, which allows for the identification of surface and confinement effects on the susceptibility. This decomposition reveals that the occurrence of confinement effects is practically independent of frequency and limited to systems with confinement length of less than 1.4 nm. Based on this analysis, we discuss the relation between the electric susceptibility and the microscopic structure and dynamics of interfacial and nanoconfined water. In particular, we discuss five different features of the water spectrum: the 15 GHz Debye peak, which is caused by molecular rotations, the 5 THz hydrogen bond stretch peak, the 20 THz libration peak due to hindered

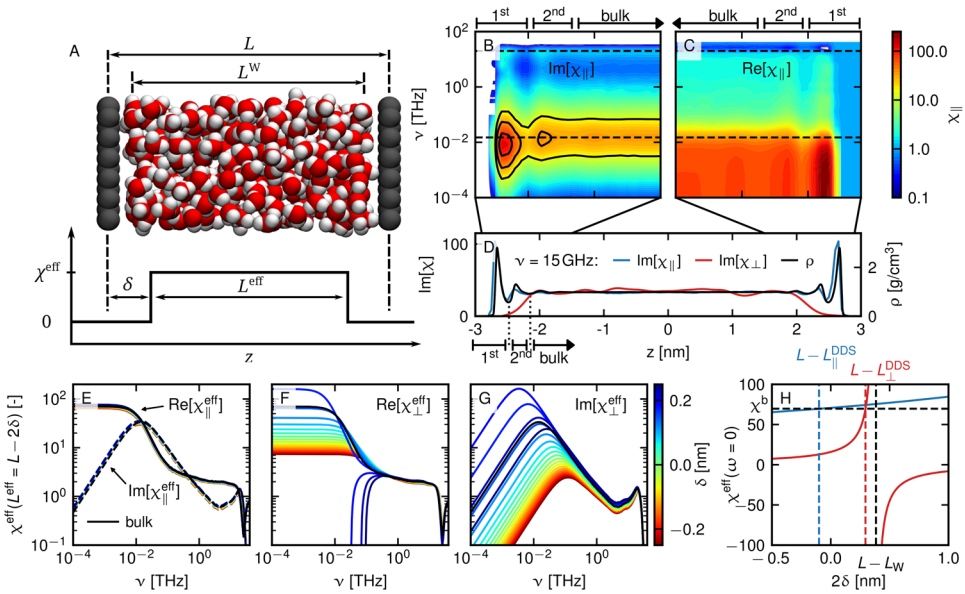

FIG. 1. Spatially dependent susceptibilities of water between two graphene sheets from FF-MD simulations. (a) Snapshot from a system with graphene sheet separation $L = 3.4$ nm and sketch of the box model used to define the effective susceptibilities χ^{eff}. Spatially dependent susceptibility: imaginary (b) and real (c) parts of the parallel susceptibility $\chi_\parallel$ of the $L = 6.0$ nm system in the first 1.5 nm at the interface. The positions of the bulk Debye peak (15 GHz) and libration peak (20 THz) are denoted as horizontal dashed lines. (d) Parallel $\chi_\parallel$ (blue line) and perpendicular $\chi_\perp$ (red line) components of the imaginary part of the susceptibility at 15 GHz of the $L = 6.0$ nm system compared to the corresponding mass density profile ρ (black line). $\chi_\perp$ is smoothed with a Gaussian kernel of width 1.5 Å. (e)–(g) Effective parallel and perpendicular dielectric susceptibilities of the $L = 6.0$ nm system for different effective lengths $L^{\text{eff}} = L - 2\delta$ according to the box model sketched in panel (a) and defined in Eqs. (11) and (12). The bulk spectrum is denoted by the black lines. (h) Effective parallel and perpendicular static susceptibility $\chi_\alpha^{\text{eff}}(\omega = 0)$ of the $L = 6.0$ nm system as a function of the effective shift $\delta = (L - L^{\text{eff}})/2$. The horizontal dashed line denotes the static bulk susceptibility of SPC/E water $\chi^{\text{b}} = 69.7$. The vertical dashed lines indicate 2δ for the specific effective lengths L_{W} (black) and L_α^{DDS} (red and blue), with L_α^{DDS} being the distances between the dielectric dividing surfaces according to Eq. (13).

rotations, the 50 THz HOH bend, and the 100 THz OH stretch peak.

When going from bulk to confinement, we find a redshift of the 15 GHz Debye peak consistent with the experimental results for hydrated solutes[41,42] and a blueshift of the 100 THz OH stretch peak, which has been found experimentally in different interfacial systems.[6,7,12,15] In contrast, the 50 THz HOH bend peak red shifts in confinement. Our analysis reveals that all these effects are predominantly interfacial effects, with geometrical confinement only tuning their strength. Finally, we discuss the hydrogen-bond network of interfacial and nanoconfined water in terms of the hydrogen-bond stretch peak around 5 THz and the libration peak around 20 THz. This reveals a confinement-induced transition of the bulk libration band to a broad absorbance band spanning from 1 to 30 THz, providing a spectroscopic fingerprint of spatially extended two-dimensional water layers.

II. RESULTS

We conduct force-field (FF) molecular dynamics (MD) simulations of SPC/E water[43] confined between two graphene sheets, as schematized in Fig. 1(a). We study four different graphene sheet separations L = 0.7, 1.4, 3.4, and 6.0 nm, containing 212, 627, 1874, and 3489 water molecules, respectively. The simulation boxes have lateral sizes of 4.26×4.43 nm^2. For the separations L = 0.7, 1.4, and 3.4 nm, we also conduct density functional theory (DFT) MD simulations using lateral box dimensions of 2.71×2.98, 2.71×2.98, and 1.97×2.13 nm^2, containing 90, 268, and 416 water molecules, respectively. The numbers of water molecules N_W are fixed at values that reproduce the chemical potential of bulk SPC/E water and have been determined in an earlier work.[37] With the specific bulk water volume $v_W = 0.030\,36$ nm^3, which we determined from bulk SPC/E simulations in the NpT ensemble at p = 1 bar at T = 300 K, the number of water molecules defines the water layer volume $V_W = L_W A$ as well as the water layer thickness L_W as

$$L_W = N_W v_W / A, \tag{1}$$

which we use to quantify the degree of confinement. Here, A refers to the lateral simulation box area. In agreement between FF-MD and DFT-MD, mass density profiles shown in Fig. 1(d) (L = 6.0 nm FF-MD) and Figs. 2(a)–2(c) (L = 0.7, 1.4, and 3.4 nm comparison between FF-MD and DFT-MD) show pronounced layering in a region of ~0.5 nm at the interface. For $L \geq 1.4$ nm, we can define two hydration layers of 0.52 and 0.34 nm thickness [based on the first and second minima of the mass density profile of the L = 6.0 nm system; see Fig. 1(d)]. The smallest system under consideration hosts only a single layer of two-dimensionally arranged water molecules. See the supplementary material, Sec. S1 for further snapshots of the simulated systems.

A. Position-dependent electric susceptibilities

In general, the spectral response of water to an external frequency-dependent field is tensorial and nonlocal. On the linear level, the electric field $\tilde{\mathbf{E}}(\mathbf{r}, \omega)$ and the electric displacement field $\tilde{\mathbf{D}}(\mathbf{r}, \omega)$ are connected by the nonlocal tensorial response function as

$$\tilde{\mathbf{D}}(\mathbf{r}, \omega) = \varepsilon_0 \int \mathrm{d}\mathbf{r}'\, \varepsilon_{\mathrm{nl}}(\mathbf{r}, \mathbf{r}', \omega) \tilde{\mathbf{E}}(\mathbf{r}', \omega). \tag{2}$$

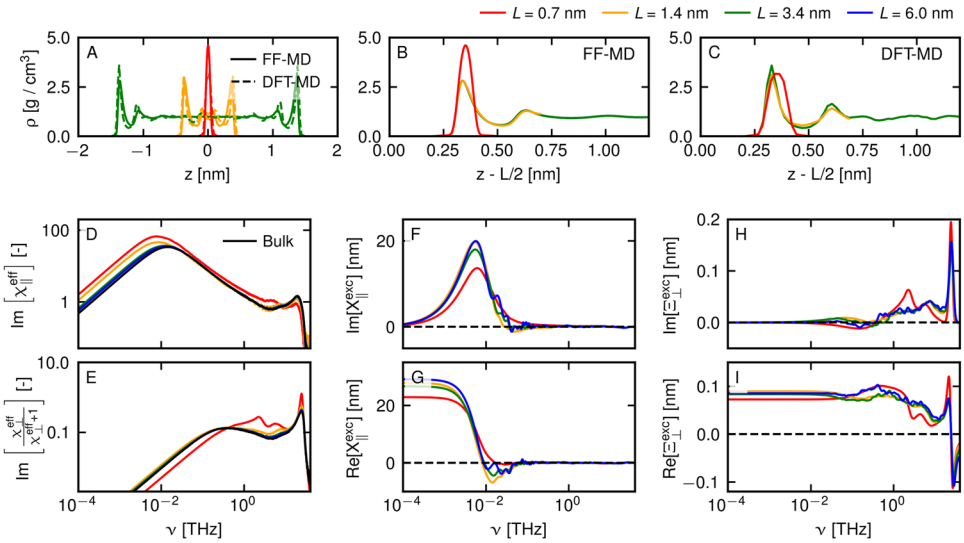

FIG. 2. Influence of confinement length on different water properties. (a) Mass density profiles of water between two graphene sheets at different separations L. The FF-MD results (solid lines) are compared to the DFT-MD results (dashed lines). The profiles are shifted with respect to the graphene sheet position in (b) (FF-MD) and (c) (DFT-MD). It should be noted that in panel (b), the blue line for the L = 6.0 nm system is exactly hidden behind the green line. (d) and (e) Imaginary part of the effective response functions for $L^{\mathrm{eff}} = L_W$ of the parallel and perpendicular component for different graphene sheet separations from FF-MD simulations. The bulk spectrum is denoted by the black lines. (f)–(i) Excess spectra according to Eqs. (14) and (15) of systems with different graphene sheet separation from FF-MD simulations.

A similar equation relates $\tilde{\mathbf{E}}(\mathbf{r},\omega)$ to $\tilde{\mathbf{D}}(\mathbf{r},\omega)$ using the functional inverse $\varepsilon_{\mathrm{nl}}^{-1}(\mathbf{r},\mathbf{r}',\omega)$. In planar interfacial systems, the laterally averaged electric and displacement fields are only functions of the interfacial normal coordinate z and the response function becomes diagonal with a parallel ($\parallel$) and a perpendicular ($\perp$) component. Under the assumption that magnetic fields can be neglected, i.e., assuming that the penetration depth of incoming electromagnetic radiation is much larger than the spatial variation of the interfacial properties, the perpendicular displacement field $\tilde{D}_\perp(z,\omega) = \tilde{D}_\perp(\omega)$ and the parallel electric field $\tilde{E}_\parallel(z,\omega) = \tilde{E}_\parallel(\omega)$ can be considered constant in space.[22] From Eq. (2), we define the integrated dielectric functions[22] $\varepsilon_\parallel(z,\omega) = \int \mathrm{d}\mathbf{r}'\ \varepsilon_{\mathrm{nl},\parallel}(z,\mathbf{r}',\omega)$ and $\varepsilon_\perp^{-1}(z,\omega) = \int \mathrm{d}\mathbf{r}'\ \varepsilon_{\mathrm{nl},\perp}^{-1}(z,\mathbf{r}',\omega)$. Using these local response functions, the following exact response relations hold

$$\tilde{\mathbf{D}}_\parallel(z,\omega) = \varepsilon_0\varepsilon_\parallel(z,\omega)\tilde{\mathbf{E}}_\parallel(\omega), \tag{3}$$

$$\tilde{E}_\perp(z,\omega) = \varepsilon_0^{-1}\varepsilon_\perp^{-1}(z,\omega)\tilde{D}_\perp(\omega). \tag{4}$$

Accordingly, we define the local electric susceptibilities as

$$\chi_\parallel(z,\omega) = \varepsilon_\parallel(z,\omega) - 1, \tag{5}$$

$$\chi_\perp(z,\omega) = \frac{1}{\varepsilon_\perp^{-1}(z,\omega)} - 1, \tag{6}$$

so that the frequency-dependent polarization density $\tilde{\mathbf{m}}(z,\omega)$, which is the relevant observable of spectroscopic measurements, is related to the electric field according to $\tilde{\mathbf{m}}_\parallel(z,\omega) = \varepsilon_0\chi_\parallel(z,\omega)\tilde{\mathbf{E}}_\parallel(\omega)$ and $\tilde{m}_\perp(z,\omega) = \varepsilon_0\chi_\perp(z,\omega)\tilde{E}_\perp(z,\omega) = \frac{\chi_\perp(z,\omega)}{\chi_\perp(z,\omega)+1}\tilde{D}_\perp(\omega)$. It should be noted that the standard relation $\tilde{\mathbf{m}}(z,\omega) = \tilde{\mathbf{D}}(z,\omega) - \varepsilon_0\tilde{\mathbf{E}}(z,\omega)$ still holds in both parallel and perpendicular directions. From our MD simulations, we determine the parallel and perpendicular components of the complex susceptibility using the Green–Kubo relations[44,45] (see the supplementary material, Sec. S2 for a derivation including electronic polarizabilities),

$$\chi_\parallel(z,\omega) = \frac{\phi_\parallel(z,0) + i\omega\tilde{\phi}_\parallel^+(z,\omega) + a_\parallel(z)}{2\varepsilon_0 k_B T}, \tag{7}$$

$$\frac{\chi_\perp(z,\omega)}{\chi_\perp(z,\omega)+1} = \frac{\phi_\perp(z,0) + i\omega\tilde{\phi}_\perp^+(z,\omega) + a_\perp(z)}{\varepsilon_0 k_B T + (\Phi_\perp(0) + i\omega\tilde{\Phi}_\perp^+(\omega) + A_\perp)/V}, \tag{8}$$

where we define the Fourier transform $\tilde{f}(\omega) = \int_{-\infty}^{\infty} \mathrm{d}t\ e^{i\omega t} f(t)$ and the one-sided Fourier transformation $\tilde{f}^+(\omega) = \int_0^{\infty} \mathrm{d}t\ e^{i\omega t} f(t)$, as well as the polarization autocorrelation functions,

$$\phi_\alpha(z,t) = \langle \mathbf{m}_\alpha(z,0)\cdot\mathbf{M}_\alpha(t)\rangle - \langle \mathbf{m}_\alpha(z)\rangle\cdot\langle\mathbf{M}_\alpha\rangle, \tag{9}$$

$$\Phi_\alpha(t) = \langle \mathbf{M}_\alpha(0)\cdot\mathbf{M}_\alpha(t)\rangle - \langle \mathbf{M}_\alpha\rangle\cdot\langle\mathbf{M}_\alpha\rangle, \tag{10}$$

for $\alpha = \parallel, \perp$. Here, $\mathbf{m}_\alpha(z,t)$ denotes the polarization density profile parallel ($\alpha = \parallel$) or perpendicular ($\alpha = \perp$) to the interface and $\mathbf{M}_\alpha(t) = \int_V \mathrm{d}\mathbf{r}\ \mathbf{m}_\alpha(z,t)$ is the total dipole moment of the simulation box of volume V. For instantaneously polarizable systems, as is the case for Born–Oppenheimer DFT-MD, the position-dependent electronic polarizability $a_\alpha(z)$ and the total system electronic polarizability $A_\alpha = \int_V \mathrm{d}\mathbf{r}\ a_\alpha(z)$ in Eqs. (7) and (8) have to be taken into account, while in the case of nonpolarizable FF-MD simulations, they are zero. As detailed in the methods section, in case of DFT-MD simulations, we determine A_α from separate simulations with explicitly applied electric fields.

In Figs. 1(b) and 1(c), we show $\chi_\parallel(z,\omega)$ from FF-MD simulation of the system with the largest separation under study ($L = 6$ nm) as a function of both position and frequency. At all distances from the interface, we observe the Debye and the libration peak in the imaginary component [Fig. 1(b)] close to their respective bulk positions, as denoted by the horizontal black dashed lines. It should be noted that the hydrogen-bond stretch feature, which is usually located in between the Debye and libration feature around 5 THz, is known to be missing for the SPC/E model because it is a fixed charge model.[46] In the Debye regime, $\mathrm{Im}[\chi_\parallel(z,\omega)]$ is bulk-like for $z > 0.9$ nm and varies closer to the interface, as highlighted by the contour lines shown in Fig. 1(b).

In Fig. 1(d), we plot the cross section of $\chi_\parallel(z,\omega)$ at the bulk frequency of the Debye peak ($\nu = 15$ GHz) and overlay it with the perpendicular susceptibility $\chi_\perp(z,\omega)$ as well as the mass density profile (black line). We observe that in the parallel case (blue line), the intensity of the Debye mode varies approximately proportionally to the water density (black line), while the perpendicular component (red line) is strongly suppressed in the interfacial region. The Debye peak of $\mathrm{Im}[\chi_\parallel(z,\omega)]$ is both enhanced and red shifted in the first hydration layer [see Fig. 1(b), contour lines], as will be discussed in more detail in the following.

B. Dielectric box model

In typical experiments, the position dependence of the electric susceptibility cannot be resolved. Instead, the spatially integrated absorption, reflectivity or capacitance of a system is measured. The interpretation of such experimental data, therefore, relies on the comparison with an effective spectrum of the system that results from a box-model shown in Fig. 1(a) and was previously introduced in the static limit.[29,37] The box model is constructed such that the integrated frequency-dependent polarization $\tilde{\mathbf{M}}(\omega)$ stays invariant (see the supplementary material, Sec. S3 for more information). We thus introduce the effective susceptibility $\chi^{\mathrm{eff}}(\omega)$ and the effective dielectric length L^{eff} according to

$$\frac{\tilde{M}_\parallel(\omega)}{\varepsilon_0 A\tilde{E}_\parallel(\omega)} = \int_{-\infty}^{\infty} \mathrm{d}z\ \chi_\parallel(z,\omega) \equiv L_\parallel^{\mathrm{eff}}\chi_\parallel^{\mathrm{eff}}(\omega), \tag{11}$$

$$\frac{\tilde{M}_\perp(\omega)}{A\tilde{D}_\perp(\omega)} = \int_{-\infty}^{\infty} \mathrm{d}z\ \frac{\chi_\perp(z,\omega)}{\chi_\perp(z,\omega)+1} \equiv L_\perp^{\mathrm{eff}}\frac{\chi_\perp^{\mathrm{eff}}(\omega)}{\chi_\perp^{\mathrm{eff}}(\omega)+1}. \tag{12}$$

It should be noted that A here denotes the lateral simulation box area (and not the polarizability). The perpendicular effective susceptibility $\chi_\perp^{\mathrm{eff}}(\omega)$ is significantly influenced by the choice of dielectric

length $L_\perp^{\text{eff}}$. In Figs. 1(e)–1(g), we show imaginary and real parts of the effective parallel and perpendicular dielectric susceptibilities for different $L^{\text{eff}} = L - 2\delta$, where δ denotes the interfacial dielectric shift. While the parallel $\chi_\parallel^{\text{eff}}(\omega)$ is only weakly modified, the perpendicular effective susceptibility $\chi_\perp^{\text{eff}}(\omega)$ changes drastically upon changing the effective length $L_\perp^{\text{eff}}$ by only a few angstroms. This impact is most pronounced in the static limit: The static dielectric constant $\varepsilon_\perp^0 = 1 + \chi_\perp^{\text{eff}}(\omega = 0)$ is calculated to be $\varepsilon_\perp^0 = 15.9$ for $L_\perp^{\text{eff}} = L$, while with $L_\perp^{\text{eff}} = L - 0.3$ nm, the SPC/E bulk dielectric constant of $\varepsilon_\perp^0 = 70.7$ is retrieved, as was shown in earlier works.[36,37] The specific effective length L_α^{DDS} that reproduces the bulk dielectric constant in the static limit was previously interpreted as the distance between the two dielectric dividing surfaces of the confined system, defined at a single interface according to[47]

$$z_\alpha^{\text{DDS}} = z_s + \int_{z_s}^{z_l} \mathrm{d}z \frac{m_\alpha(z_l, \omega = 0) - m_\alpha(z, \omega = 0)}{m_\alpha(z_l, \omega = 0) - m_\alpha(z_s, \omega = 0)}, \tag{13}$$

with z_s and z_l being positions deep in the solid and liquid phase, respectively.

Determining the perpendicular effective susceptibility for an ill-chosen effective length can, therefore, result in misleading interpretations when trying to describe the influence of confinement on the susceptibility of water. As an example, a common approach is to choose $L^{\text{eff}} = L_W$. This is suitable for the parallel component for all frequencies but for the perpendicular component only in the THz and IR region where $\chi_\perp^{\text{eff}}$ is small and thus $\frac{\chi_\perp^{\text{eff}}}{\chi_\perp^{\text{eff}}+1} \approx \chi_\perp^{\text{eff}}$. However, for the perpendicular component at low frequencies, choosing $L_\perp^{\text{eff}} = L_W$ leads to an unintuitive negative value for the effective static dielectric constant. The dependence of $\chi_\alpha^{\text{eff}}(\omega = 0)$ on the choice of effective length is shown in Fig. 1(h). It shows that varying δ in a range of only 0.4 Å, we recover the bulk behavior at $L_\perp^{\text{eff}} = L_\perp^{\text{DDS}}$ ($\delta = 0.15$ nm), find a diverging effective susceptibility at $\delta = 0.17$ nm and a negative effective susceptibility at $L_\perp^{\text{eff}} = L_W$ ($\delta = 0.19$ nm).

One way to circumvent the high sensitivity of the perpendicular effective susceptibility $\chi_\perp^{\text{eff}}$ on the effective length $L_\perp^{\text{eff}}$ is to report the response function to the displacement field $\frac{\chi_\perp^{\text{eff}}}{\chi_\perp^{\text{eff}}+1}$ instead, which is rather well behaved, as follows from Eq. (12) (see the supplementary material, Sec. S3). In fact, $\frac{\chi_\perp^{\text{eff}}}{\chi_\perp^{\text{eff}}+1}$ is the experimentally measured response function for energy absorption of the radiation component with electric field perpendicular to the interface (see the supplementary material, Sec. S5 for a derivation of the transmittance coefficient of spectroscopic transmission experiments). Therefore, to interpret our spectra in a robust and experimentally relevant fashion, we systematically analyze $\frac{\chi_\perp^{\text{eff}}}{\chi_\perp^{\text{eff}}+1}$ for all FF simulations.

C. Bulk-interface-confinement decomposition

To separate interfacial from confinement effects of nanoconfined water, we compare effective response functions $\chi_\parallel^{\text{eff}}$ and $\frac{\chi_\perp^{\text{eff}}}{\chi_\perp^{\text{eff}}+1}$ calculated for systems with different graphene sheet separation L shown in Figs. 2(d) and 2(e). In general, the effective response becomes more and more bulk-like with increasing L. In the parallel component shown in Fig. 2(d), in agreement with experimental measurements,[13,17] a redshift of the Debye peak around 15 GHz is observed when going from bulk to confinement. At the same time, the magnitude of the libration peak around 20 THz decreases. In the perpendicular component, only minor changes in the Debye region are observed for system sizes larger than $L = 0.7$ nm, while the Debye response is slightly lowered for the smallest system. In the libration region, the intensity increases when going from bulk to confinement.

We seek to relate spectral changes to either the effect that a single interface has on the structure and dynamics of water or to the effect of geometrical confinement between two interfaces. A first signature of interfacial and confinement effects can be illustrated with the mass density profiles shown in Figs. 2(b) and 2(c): As has been vastly discussed in the literature, water has a nonuniform density in the vicinity of interfaces. When we superpose the density profiles of systems with different confinement lengths and shift them to a common origin, the resulting profiles are practically identical for systems with $L \geq 1.4$ nm, i.e., the density variations are independent of confinement length and thus of interfacial nature. Only when going to even smaller lengths, the density profile deviates and confinement effects become relevant. Indeed, for the smallest system with $L = 0.7$ nm, we have only a single sheet of water between the two graphene sheets and the density profile shows a single higher and broader peak.

In order to quantify interfacial and confinement effects on the frequency-dependent response in a consistent and robust manner, we decompose the total polarization $\tilde{\mathbf{M}}_\alpha(\omega)$ into a bulk part $V_W \tilde{\mathbf{m}}_\alpha^{\text{b}}(\omega)$ and an excess part $\tilde{\mathbf{M}}_\alpha^{\text{exc}}(\omega, L)$, which depends parametrically on L, where the bulk polarization is defined by the water bulk susceptibility $\chi^{\text{b}}(\omega)$ according to $\tilde{\mathbf{m}}_\parallel^{\text{b}}(\omega) = \varepsilon_0 \chi^{\text{b}}(\omega) \tilde{\mathbf{E}}_\parallel(\omega)$ or $\tilde{m}_\perp^{\text{b}}(\omega) = \frac{\chi^{\text{b}}(\omega)}{\chi^{\text{b}}(\omega)+1} \tilde{D}_\perp(\omega)$. This results into the decomposition of the polarization response according to

$$\frac{\tilde{M}_\parallel(\omega)}{\varepsilon_0 A \tilde{E}_\parallel(\omega)} = L_\parallel^{\text{eff}} \chi_\parallel^{\text{eff}}(\omega) = L_W \chi^{\text{b}}(\omega) + X_\parallel^{\text{exc}}(\omega, L), \tag{14}$$

$$\frac{\tilde{M}_\perp(\omega)}{A \tilde{D}_\perp(\omega)} = L_\perp^{\text{eff}} \frac{\chi_\perp^{\text{eff}}}{\chi_\perp^{\text{eff}} + 1} = \frac{L_W \chi^{\text{b}}(\omega)}{1 + \chi_\perp^{\text{b}}(\omega)} + \Xi_\perp^{\text{exc}}(\omega, L). \tag{15}$$

In agreement with the mass density profiles shown in Figs. 2(b) and 2(c), the excess response functions $X_\parallel^{\text{exc}}(\omega, L) = \frac{\tilde{M}_\parallel^{\text{exc}}(\omega, L)}{\varepsilon_0 A \tilde{E}_\parallel(\omega)}$ and $\Xi_\perp^{\text{exc}}(\omega, L) = \frac{\tilde{M}_\perp^{\text{exc}}(\omega, L)}{A \tilde{D}_\perp(\omega)}$ shown in Figs. 2(f)–2(i) converge to a common function for $L \geq 1.4$ nm, although we observe slight deviations due to data uncertainty. For $L = 0.7$ nm, however, the excess response functions clearly deviate, indicating an onset of confinement effects below $L = 1$ nm, consistent with previous results for the static dielectric constant.[29,37]

The excess response functions $X_\parallel^{\text{exc}}$ and $\Xi_\perp^{\text{exc}}$ can be further decomposed into interface and confinement contributions, according to

$$X_\parallel^{\text{exc}}(\omega, L) = 2X_\parallel^{\text{int}}(\omega) + X_\parallel^{\text{conf}}(\omega, L), \tag{16}$$

$$\Xi_\perp^{\text{exc}}(\omega, L) = 2\Xi_\perp^{\text{int}}(\omega) + \Xi_\perp^{\text{conf}}(\omega, L). \tag{17}$$

For large confinement length, the confinement contribution goes to zero, $X_{\parallel}^{conf}(\omega, L \to \infty) \to 0$, which allows us to define $X_{\parallel}^{int}(\omega) = \frac{1}{2}X_{\parallel}^{exc}(\omega, L \to \infty)$ (likewise for the perpendicular response function). In practice, in case of the FF-MD results, the interface excess is chosen to be half the total excess response function of the $L = 6.0$ nm system $X_{\parallel}^{int}(\omega) = \frac{1}{2}X_{\parallel}^{exc}(\omega, L = 6.0\ \text{nm})$ and $\Xi_{\perp}^{int}(\omega) = \frac{1}{2}\Xi_{\perp}^{exc}(\omega, L = 6.0\ \text{nm})$. The resulting interface and confinement excess spectra are shown in Figs. 3(c)–3(f). While the interface contribution is unique for the graphene–water interface, the confinement excess spectrum depends on the graphene sheet separation L. Here, we only show the confinement spectrum corresponding to $L = 0.7$ nm.

The interface excess (see Fig. 3 blue lines) is pronounced in all spectral regions. As a reference, the frequencies of the major bulk SPC/E spectral features (15 GHz Debye peak and 20 THz libration peak) are depicted by the vertical black dashed lines. In the parallel component, the redshift of the Debye mode shown in Fig. 2(d) can be assigned to an interfacial effect, as seen from the pronounced positive peak in the imaginary part in Fig. 3(c) located at a frequency lower than the bulk Debye frequency. This redshift goes hand in hand with an overall increase in intensity, which is reflected in the positive static interface excess susceptibility $X_{\parallel}^{int}(\omega = 0) = 12.5$ nm [Fig. 3(d) plateau of the blue line at low frequencies]. On the other hand, the parallel libration feature at 20 THz is decreased due to the interface [see the blue line in the inset of Fig. 3(c)]. The perpendicular component of the interface excess [Fig. 3(e), blue line] is small in the GHz regime, but has a sharp positive peak located at a frequency slightly higher than the center frequency of the bulk libration peak at 20 THz.

In order to pinpoint the origin of the interface spectra shown in Figs. 3(c)–3(f), we decompose the interface excess spectra $X_{\parallel}^{int}$ and $\Xi_{\perp}^{int}$ into contributions from the first and second hydration layers at the interface of the $L = 6.0$ nm system [see Fig. 1(d) for definition of hydration layers]. These contributions are shown in Fig. 3, indicated by the dashed and dotted blue lines, respectively: We observe that nearly the entire interface excess stems from the first hydration layer (see Sec. S3 of the supplementary material for more information).

In the confinement excess shown in Fig. 3 (red lines), we observe a confinement-induced blue shift of the parallel component of the Debye peak shown in Fig. 3(c), which counteracts the interfacial redshift at the graphene surface. This blue shift does not include a major change in intensity, reflected by the small static confinement excess of $X_{\parallel}^{conf}(\omega = 0) = -1.95$ nm shown in Fig. 3(d). In the perpendicular component, the sharp feature in the vicinity of the libration peak is enhanced due to confinement [see Fig. 3(e)], which leads to overscreening in the frequency regime between 25 and 28 THz, i.e., the real part of the perpendicular response $\frac{\chi_{\perp}^{eff}}{\chi_{\perp}^{eff}+1}$ of single layer water becomes negative (see the supplementary material, Sec. S3). Such overscreening is well known for the nonlocal dielectric response of liquid bulk water in certain wave number regimes[48,49] and for the static perpendicular response of confined water in a thin interfacial layer,[50] but not for the macroscopic response of entire aqueous systems.

Notably, a new peak emerges at around 2 THz in the perpendicular component as a result of strong confinement in Fig. 3(e). Since this is in the frequency range of hydrogen bond stretch modes, which are not faithfully described by the SPC/E model, we will discuss this feature in Sec. II E with the help of DFT-MD simulations.

The interpretation of the confinement excess becomes clearer by comparing it with the dielectric response of the first layer of water in the $L = 6.0$ nm system. In Fig. 3(c), we observe that interfacial and confinement excess are almost opposite (represented by the solid red line for confinement excess vs the dashed blue line for first hydration layer). This indicates that the dielectric behavior of a single confined water layer is rather similar to the behavior of the interfacial layer of the $L = 6.0$ nm system. This interpretation stems from the definition of the confinement excess in Eqs. (16) and (17). There, we subtract the interface excess twice. Thus, a confinement excess of a single water layer that is equal to the negative of the interface excess, as is the case in the Debye region, indicates a similar dielectric response of the interfacial and confined layers. A vanishing confinement excess, however, would indicate that the confined layer is approximately twice as dielectrically active as the first hydration layer at the interface, which in fact is the case for the libration feature [see Fig. 3(c), red line in the inset].

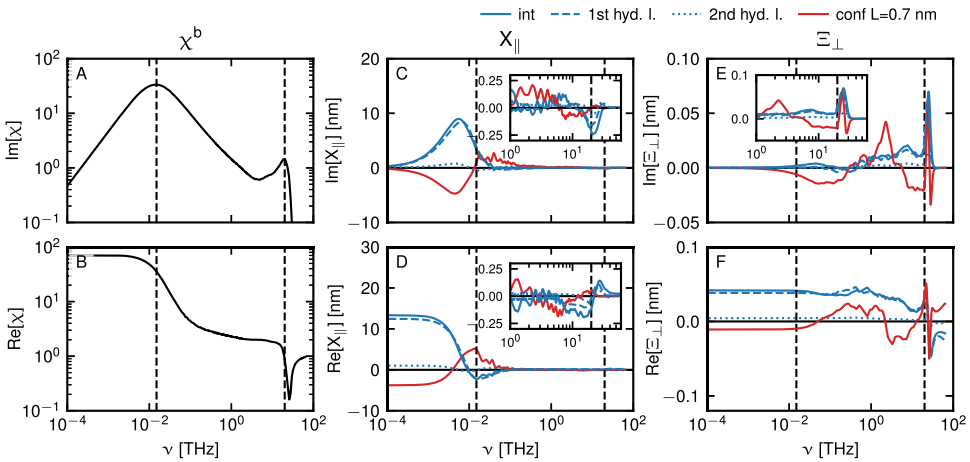

FIG. 3. Decomposition of FF-MD spectra. (a) and (b) Susceptibility spectrum of bulk water. (c)–(f) Parallel and perpendicular interfacial (blue solid) and confinement (red solid) excess response functions according to Eqs. (16) and (17). The blue dashed and dotted lines show contributions from the first and second hydration layer to the interfacial excess response function, respectively. The confinement contribution is depicted for the smallest considered system (L = 0.7 nm). The vertical dashed lines denote the bulk frequencies of the Debye and libration peak of SPC/E water at 15 GHz and 20 THz.

D. Molecular vs collective reorientations from FF-MD

Typically, the dielectric response of water is interpreted in terms of the motion of individual water molecules. However, since the reorientation of water molecules is significantly influenced by the hydrogen-bond network, the motion of neighboring water molecules is strongly correlated. In order to interpret the interface and confinement excess response functions shown in Fig. 3 on a molecular level, we decompose the polarization autocorrelation function Φ_α defined in Eq. (10) into a self-part $\Phi_\alpha^{\text{self}}$, which corresponds to single molecule rotational dynamics, and a collective contribution $\Phi_\alpha^{\text{coll}}$, which corresponds to collective orientation effects. Self and collective parts are given by

$$\Phi_\alpha^{\text{self}}(t) = \sum_{i=1}^{N_W} \left\langle \mu_i^\alpha(0)\mu_i^\alpha(t)\right\rangle, \tag{18}$$

$$\Phi_\alpha^{\text{coll}}(t) = \sum_{i\neq j}^{N_W} \left\langle \mu_i^\alpha(0)\mu_j^\alpha(t)\right\rangle, \tag{19}$$

where μ_i denotes the dipole moment of molecule i and the sum runs over all water molecules. Autocorrelation functions are Fourier transformed and rescaled by the effective dielectric length L^{eff} to obtain the self and collective contributions to the effective dielectric response functions, according to

$$\chi_\parallel^{\text{eff}}(\omega) = \frac{i\omega}{2AL_\parallel^{\text{eff}}\varepsilon_0 k_B}\left[\tilde\Phi_\parallel^{\text{self}}(\omega) + \tilde\Phi_\parallel^{\text{coll}}(\omega)\right], \tag{20}$$

$$\frac{\chi_\perp^{\text{eff}}(\omega)}{\chi_\perp^{\text{eff}}(\omega)+1} = \frac{i\omega}{AL_\perp^{\text{eff}}\varepsilon_0 k_B T}\left[\tilde\Phi_\perp^{\text{self}}(\omega) + \tilde\Phi_\perp^{\text{coll}}(\omega)\right]. \tag{21}$$

This decomposition is shown in Fig. 4 for $L_\parallel^{\text{eff}} = L_\perp^{\text{eff}} = L_W$.

The parallel component of the self-part [Fig. 4(a) solid lines] shows a red shift of the Debye peak when going from bulk to confinement, i.e., molecular reorientation is slowed down due to the presence of the graphene sheets. The intensity of the Debye peak, however, is dominated by collective reorientations [Fig. 4(a) dashed lines]. The red shift of the absorption spectrum in the presence of graphene sheets, visible in Fig. 2(d) and in the parallel interface excess response function in Fig. 3(c), therefore, is due to a slowdown of collective reorientation in the interfacial hydrogen-bond network, while the increase in intensity is related to an increased orientational correlation of neighboring interfacial water molecules.

In Figs. 4(b) and 4(c), we show the self-collective decomposition of the perpendicular component. For all graphene separations, the self and collective contributions are nearly equal in amplitude but opposite in sign. This results in a compensation of the single molecular motion by collective anti-correlated reorientations, leading to the very small perpendicular response in the GHz range shown in Fig. 3(e) for both interface and confinement contributions. This compensation of self and collective effects reveals the molecular mechanism by which the electrostatic boundary conditions are satisfied in the system:[29] in order to satisfy Eq. (8), the perpendicular polarization autocorrelation function $\tilde\Phi_\perp$ defined in Eq. (10) has to be suppressed since $\tilde\Phi_\perp \approx \tilde\Phi^{\text{b}}/(1+\chi^{\text{b}})$, with $\chi^{\text{b}} \gg 1$ in the GHz regime, in the limit of large systems, where $\tilde\Phi^{\text{b}}$ is

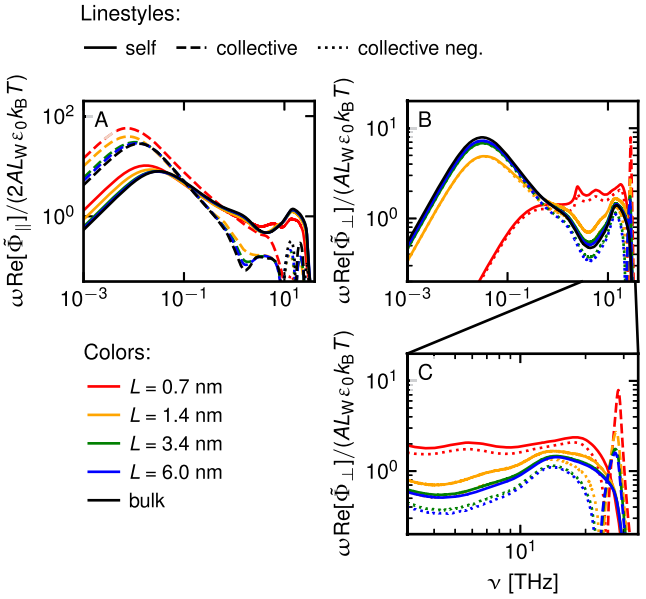

FIG. 4. Decomposition of the Fourier-transformed polarization autocorrelation function into self and collective contributions according to Eqs. (18) and (19) from FF-MD simulations normalized with respect to L_W. The normalization constant $AL_W\varepsilon_0 k_B T$ is chosen such that the sum of the self and collective contributions equals the effective dielectric response functions $\chi_\parallel^{\text{eff}}$ at $L^{\text{eff}} = L_W$ in the parallel (a) and $\frac{\chi_\perp^{\text{eff}}}{\chi_\perp^{\text{eff}}+1}$ in the perpendicular (b) component. (c) Zoom into the libration region of the perpendicular component.

the bulk autocorrelation function (see the supplementary material, Sec. S3). For systems with smaller graphene sheet separation, the Debye peak is suppressed and we see deviations from mere compensation: Notably, there is a significant increase of in-phase (positive collective) motion of water molecules around 25 THz [see Fig. 4(c)] when going from large to small systems, which causes the main features of the interfacial and confinement excess spectra shown in Fig. 3(e). The frequency at which this happens coincides with in-phase librating pairs of water molecules, which are also present in bulk water,[46] where they, however, give only a small contribution to the overall susceptibility.

E. Confined spectra from DFT-MD

The Debye peak of water gives valuable information on the reorientational dynamics of water molecules in the hydrogen-bond network.[51] Additional information can be obtained by probing the OH stretch motion around 100 THz, the HOH bending around 50 THz, and the hydrogen-bond stretch motion around 5 THz.[52,53]

Using the same methods outlined for FF-MD simulations, we determine the effective susceptibilities of water confined between graphene sheets in the IR and THz regime from DFT-MD simulations. These simulations employ the Born–Oppenheimer approximation such that the systems exhibit instantaneous electronic polarizability, which is taken into account when extracting spectra according to Eqs. (7) and (8). In Fig. 5, we show parallel and perpendicular effective absorption spectra using $L^{\text{eff}} = L_W$. It should be

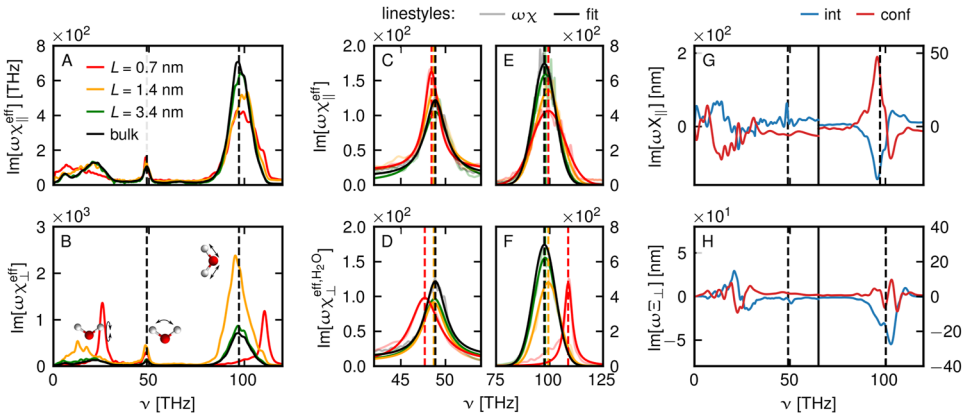

FIG. 5. Parallel (a) and perpendicular (b) components of the effective absorption spectrum for $L^{\mathrm{eff}} = L_{\mathrm{W}}$ from DFT-MD simulations for different graphene sheet separations L compared to the bulk result (black line). The HOH bend features [(c) and (d)] and OH stretch features [(e) and (f)] are shown in detail, and the raw data (transparent lines) are fitted (solid lines). The peak positions according to the fits are indicated by the vertical dashed lines. For the perpendicular spectra, the effective water susceptibility according to Eq. (22) is fitted. (g) and (h) Interface (blue lines) and confinement (red lines) excess response functions from DFT-MD simulations.

noted that in the IR regime, effective susceptibilities are rather insensitive to the choice of an effective dielectric length, so that $L^{\mathrm{eff}} = L_{\mathrm{W}}$ is suitable. This allows us to compare $\omega\mathrm{Im}[\chi^{\mathrm{eff}}]$ in both parallel and perpendicular direction to bulk absorption spectra. It should be noted that spectroscopic experiments in transmission or attenuated-total-reflection geometry actually measure $\omega\mathrm{Im}[\chi_{\parallel}^{\mathrm{eff}}]$ in the parallel component but $\omega\mathrm{Im}[\frac{\chi_{\perp}^{\mathrm{eff}}}{\chi_{\perp}^{\mathrm{eff}}+1}]$ in the perpendicular component, which then has to be converted to compare to bulk measurements (see the supplementary material, Sec. S5). Still, when comparing with the bulk susceptibility, an additional effect has to be taken into account: in case of the perpendicular component [Fig. 5(b)], the computed features are drastically larger in confinement than in bulk, in contrast to the parallel case [Fig. 5(a)]. This is caused by the presence of polarizable graphene: In analogy to what we find in Sec. II B and to what has been extensively discussed in the literature in the static limit: adding a dielectrically dead layer to the system while keeping L^{eff} constant leads to a sharp decrease in effective susceptibility,[29,38,39,50] adding the highly polarizable graphene while keeping the effective length L^{eff} constant leads to an increase in effective susceptibility, which could be misinterpreted as an increased spectral activity of the confined water. This occurs despite the fact that, within our level of description, graphene is not absorbing.

In order to define an effective susceptibility, which singles out the water dynamics, we keep $L^{\mathrm{eff}} = L_{\mathrm{W}}$, but subtract the electronic polarizability contribution of the pristine graphene sheets, denoted as $A_{\perp}^{\mathrm{graph}}$. For this, we define the effective water susceptibility by slight modification of Eq. (8) as

$$\frac{\chi_{\perp}^{\mathrm{eff,H_2O}}(\omega)}{\chi_{\perp}^{\mathrm{eff,H_2O}}(\omega)+1} = \frac{(\Phi_{\perp}(0) + i\omega\tilde{\Phi}_{\perp}^{+}(\omega) + \langle A_{\perp}\rangle - \langle A_{\perp}^{\mathrm{graph}}\rangle)/V_{\mathrm{W}}}{\varepsilon_0 k_B T + (\Phi_{\perp}(0) + i\omega\tilde{\Phi}_{\perp}^{+}(\omega) + \langle A_{\perp}\rangle)/V}. \tag{22}$$

In the supplementary material, Sec. S4, we show that this corresponds, in good approximation, to the response function of the water polarization to the perpendicular displacement field, i.e., $\tilde{M}_{\perp}^{\mathrm{H_2O}}(\omega) \approx L^{\mathrm{eff}} \frac{\chi_{\perp}^{\mathrm{eff,H_2O}}(\omega)}{\chi_{\perp}^{\mathrm{eff,H_2O}}(\omega)+1} \tilde{D}_{\perp}(\omega)$ when decomposing the total polarization into a water and a graphene contribution $\tilde{\mathbf{M}}(\omega) = \tilde{\mathbf{M}}^{\mathrm{H_2O}}(\omega) + \tilde{\mathbf{M}}^{\mathrm{graph}}(\omega)$.

The parallel total susceptibility and the perpendicular effective water susceptibility are shown for the bending and stretching modes in Figs. 5(c)–5(f). Bend peaks and stretch peaks are fitted by Lorentzian and Gaussian functions, respectively, to determine peak positions, indicated by the vertical dashed lines, and linewidths. The perpendicular confined OH stretch peak [Fig. 5(f) red line] is fitted with a Lorentzian as well. Fit parameters are detailed in the supplementary material, Sec. S6. We find qualitatively similar behavior of the parallel effective total susceptibility and the perpendicular effective water susceptibility: In both cases, the OH stretch peak around 100 THz shown in Figs. 5(e) and 5(f) undergoes a blueshift when going from bulk to strongly confined systems, consistent with IR and Raman measurements of water confined in silica nanopores.[7,16] For a single water layer ($L = 0.7$ nm), the perpendicular OH stretch peak is blueshifted to 108 THz and the linewidth is greatly reduced, corresponding to the vibration of non-hydrogen-bonded OH groups. The existence of such dangling OH groups at interfaces has been reported and discussed in detail in many interfacial systems.[54–56] In addition, we find that the intensity of the OH stretch peak, determined by the integrated area of the peak, decreases with decreasing graphene sheet separation.

The HOH bend feature in Figs. 5(c) and 5(d) shows opposite behavior that, however, is similar in the parallel and perpendicular directions. In both cases, the peak is redshifted when going from bulk to confinement. We observe a decrease in linewidth in the parallel effective susceptibility in the HOH bend region as the graphene sheet separation decreases but not in the perpendicular component. The THz region between 0 and 30 THz will be discussed in more detail in Sec. II F.

As done previously, we decompose the dielectric spectra into bulk and excess contributions according to Eqs. (14) and (15) and use Eqs. (16) and (17) to determine interface and confinement

excess. This decomposition is shown in Figs. 5(g) and 5(h). In the supplementary material, Sec. S4, we further show that, in agreement with FF simulations, only the $L = 0.7$ nm system has a confinement contribution to the excess response functions.

The OH stretch peak around 100 THz shows a negative interface excess in both the parallel and perpendicular components [blue lines shown in Figs. 5(g) and 5(h)] consistent with the decreased intensities observed in Figs. 5(a) and 5(b). In the parallel direction, we find that the confinement excess is approximately equal to the negative of the interface excess, indicating a vanishing confinement effect [similarly to the situation in the Debye region from FF-MD results shown in Figs. 3(c) and 3(d)]. Both the decreased intensity and the blue shift of the parallel response shown in Fig. 5(e) are, therefore, interfacial effects.

For the perpendicular component, discerning whether the blue shift of the OH stretch feature is an interfacial or confinement effect is more challenging. We integrate the interface excess response function from 80 THz to the center frequency of the OH stretch peak [dashed lines in Figs. 5(g) and 5(h)] as well as from the center frequency to 115 THz and compare the respective values (see the supplementary material, Sec. S4 for details). By this, we find that the shift of the perpendicular OH-stretch response shown in Fig. 5(f) is also an interfacial and not a confinement effect.

To the right of the large negative peak in the interface excess in Fig. 5(h), we observe a smaller positive peak around 108 THz, which corresponds to the vibration of free OH groups. Interestingly, the confinement excess in the region of hydrogen bonded OH stretch vibrations around 100 THz is small compared to the interface excess, which indicates, as discussed earlier, that confinement effects have an additional and equally important contribution as interfacial effects. Therefore, the intensity drop of the OH stretch peak shown in Fig. 5(f) for $L = 0.7$ nm is due to confinement, on top of the decrease for larger L due to interfacial effects. The same holds true in the 108 THz region, meaning that there is an additional contribution from free OH groups in confinement on top of the single interface case. To confirm this directly, we investigate the average number of hydrogen bonds per water molecule as a function of the distance to the graphene sheet in the supplementary material, Sec. 8. We find that the number of hydrogen bonds per water molecule decreases with decreasing distance to the graphene sheet, but that the decrease is stronger for the $L = 0.7$ nm nanoconfinement, consistent with the spectral signatures of free OH groups at the interface and confinement excess response functions shown in Fig. 5(h), as well as previous results in the literature.[57]

F. Relation between DFT spectra and molecular motion and vibrations

To interpret the interface and confinement excess spectra shown in Figs. 5(g) and 5(h) in terms of molecular vibrations, we

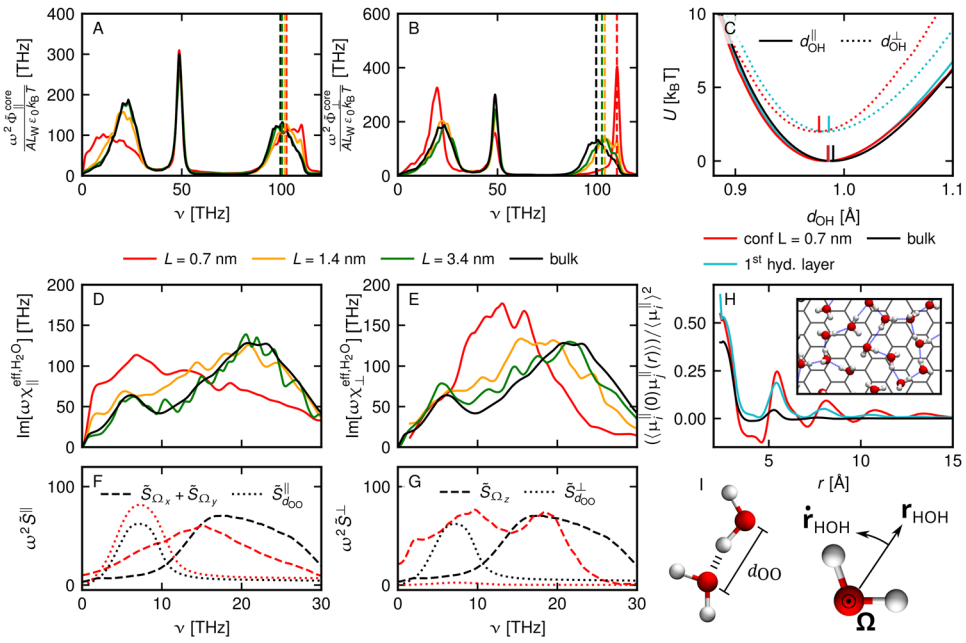

FIG. 6. Relation of interface and confinement excess spectra from DFT-MD simulations with the microscopic water structure and dynamics. (a) and (b) Parallel and perpendicular core-charge spectra according to Eq. (10), where SPC/E partial charges are placed on atomic cores. The dashed lines in panel (a) denote the position of the main OH stretch peak. (c): OH bond potential for the confined $L = 0.7$ nm system (red lines); the first hydration layer of the $L = 3.4$ nm system (cyan lines) compared to bulk (black lines). (d) and (e) Parallel and perpendicular components of the effective susceptibilities for $L^{\text{eff}} = L_W$ in the THz regime for different graphene sheet separations L. For the perpendicular component, we subtract the graphene sheet electronic polarizability. (f) and (g) Power spectra $\tilde{S}_{\boldsymbol{\Omega}}$ of the angular velocity (dashed lines) of water molecules and $\tilde{S}_{d_{OO}}$ of the oxygen–oxygen distance of hydrogen-bonded water molecules (dotted lines). (h) Radial cross-correlation function of parallel molecular orientations as quantified by molecular dipole moments μ_i (calculated at fixed core charges) (i): Sketches defining the hydrogen bond distance d_{OO}, the molecular bisector $\mathbf{r}_{HOH}$, and its angular velocity $\boldsymbol{\Omega}$.

determine the core-charge autocorrelation functions $\Phi_{\parallel}^{\text{core}}$ and $\Phi_{\perp}^{\text{core}}$. These are computed from DFT-MD simulations using Eq. (10) by placing SPC/E partial charges on the oxygen and hydrogen atomic cores. By construction, these core-charge autocorrelation functions reproduce the dynamics of molecular reorientation and vibrations but do not contain spectral contributions from electronic polarization, i.e., from the deformation of the electronic density.

We plot $\omega^2\tilde{\Phi}_{\alpha}^{\text{core}}/AL_W\varepsilon_0 k_B T$ in Figs. 6(a) and 6(b): both the parallel and perpendicular components of the core-charge autocorrelation function reproduce the blueshift of the OH stretch peak in the full DFT spectra shown in Fig. 5, but not its decrease in intensity. This indicates that the intensity decrease is due to an electronic polarization mechanism, in agreement with a previous theoretical work, which shows that the dipole moment of water molecules and, therefore, the transition dipole moment of the OH stretch mode decreases at interfaces due to weaker hydrogen bonding.[58] On the contrary, the blue shift of the OH stretch vibration stems from a change in molecular vibrational dynamics. It can be rationalized by looking at the effective bond potentials of OH groups, obtained from the bond length distributions, which reflect the local environment of water molecules, in particular the local hydrogen bond network.[59] In Fig. 6(c), we report the OH bond potentials for two water orientations: we distinguish between OH groups pointing perpendicular to the graphene sheet (⊥, dotted lines) and parallel (∥, solid lines). These are shown for bulk water (black line), water in the first hydration layer of the $L = 3.4$ nm system, denoted as interfacial water (cyan lines), and the single water layer in the $L = 0.7$ nm system, which we denote as confined water (red lines). We fit the effective bond potentials with a fourth-order polynomial and evaluate the equilibrium bond length and the curvature at the minimum k. First, we observe that, for OH groups perpendicular to the graphene sheet (dotted lines), the equilibrium bond-length $d_{\text{OH}}^{\perp}$ is 9.77 Å for the confined water and 9.86 Å for the interfacial water, both shorter than the bulk value of $d_{\text{OH}}^{\text{b}} = 9.90$ Å. Next, from the extracted curvatures, we estimate the frequency shift of interfacial and confined OH vibrations with respect to bulk using a harmonic oscillator model,

$$\nu_k^2 = \frac{k}{4\pi^2 m}, \tag{23}$$

where $m = 0.948$ u is the reduced mass of the OH vibrational system. Curvatures and resulting frequencies obtained from Eq. (23) are presented in Table I.

For comparison, we fit the parallel and perpendicular core spectra shown in Figs. 6(a) and 6(b) with two Gaussians representing the bonded OH population around 100 THz and the free OH population around 110 THz (see the supplementary material, Sec. S7). We retrieve a gradual blue shift of the bonded OH vibration frequency of about 5 THz, while the frequency of the free OH vibration stays constant for all systems. For the $L = 0.7$ nm system, we present in Table I the frequency of the bonded OH population peak in the parallel spectra as $\nu_{0\parallel}^{\text{core}}$ [vertical dashed lines shown in Fig. 6(a)] and that of the free OH population as $\nu_{0\perp}^{\text{core}}$. The interpretation and comparison of the potential-based frequencies ν_k with the peak positions of the effective susceptibilities ν_0^{eff} of the full DFT-MD simulation [vertical dashed lines shown in Figs. 5(e) and 5(f)] and of the core-charge autocorrelation functions ν_0^{core} is not straightforward. This is mostly due to the fact that we differentiate between bulk and interfacial water populations in the construction of the potential of mean force (PMF), while the effective (averaged) spectra contain contributions from both bulk and interfacial water. In the case of interfacial water in the $L = 3.4$ nm system, we see that the effective potential of the parallel interfacial OH bonds has a higher curvature with respect to bulk water, predicting a blue shift of about 5 THz. This qualitatively explains the resulting blue shift of the parallel core charge spectra shown in Fig. 6(a), where the relative contributions of bulk and interfacial water gradually change, i.e., the blue shift increases with decreasing confinement length. The effective potential of perpendicular free OH interfacial population yields an extracted frequency ν_k of 110 THz, which is the result of a very different local environment with no hydrogen bonds formed. In the core charge spectra in Figs. 6(a) and 6(b), we see a peak around that frequency with increasing intensity as we go from bulk to confinement. In the case of strongly confined water, i.e., for the $L = 0.7$ nm system, there is no contribution from bulk water molecules, so we can directly compare core spectra frequencies ν_0^{core} to potential-based frequencies ν_k. We retrieve similar shifts from bulk to confinement for all investigated frequencies, ν_0^{eff}, ν_0^{core}, and ν_k of around 2.5 THz in the parallel and around 10 THz in the perpendicular components, which hints to the fact that the blue shift of the bonded OH vibrations as well as of the free OH bonds is due to a change in curvature of the effective potentials. This reveals that the in-plane hydrogen bond network in the interfacial layer is weaker than that in bulk, leading to a higher potential curvature, and that,

TABLE I. Analysis of OH stretch frequencies. Curvature of OH bonds potentials shown in Fig. 6(c) from fourth-order polynomial fit is denoted as k. Frequencies ν_k are calculated with Eq. (23) and compared to the fitted frequencies of the OH stretch peak from the effective spectra shown in Figs. 5(e) and 5(f) (ν_0^{eff}) and core spectra shown in Figs. 6(a) and 6(b) (ν_0^{core}) of bulk water and nanoconfined water. We do not determine interfacial spectra from DFT-MD simulations so that we do not provide the according values.

		ν_0^{eff} (THz)	ν_0^{core} (THz)	k ($k_B T/\text{Å}^2$)	ν_k (THz)
Bulk		97.3	99.5	1.442	98.0
Interfacial water (first hyd. lay. $L = 3.4$ nm)	∥	⋯	⋯	1.589	102.9
	⊥	⋯	⋯	1.818	110.1
Confined water ($L = 0.7$ nm)	∥	99.4	102.5	1.518	100.6
	⊥	108.8	109.9	1.713	106.8

as mentioned earlier, the absence of hydrogen bonding for the out-of-plane free OH bonds leads to a further curvature increase and to a frequency shift to 106.8 THz.

In Sec. S7 of the supplementary material, we also show that the redshift of the HOH bend peak in confinement with respect to bulk, as shown in Figs. 5(c) and 5(d), can be rationalized by a decrease in curvature of the effective angular bond potential.

Finally, to probe the hydrogen-bond network more directly, usually the hydrogen-bond stretch feature around 5 THz is considered. We show close-ups of the effective water susceptibility in the 0 to 30 THz region in Figs. 6(d) and 6(e). Going from bulk to nanoconfinement changes the characteristics of the THz spectrum dramatically. In both the parallel and perpendicular components, instead of well-separated libration and hydrogen-bond stretch peaks, we see the emergence of a broad absorption band spanning from 1 all the way to 30 THz. A similar signature has been reported previously in single-molecule polarization power spectra of nanoconfined water.[30] The excess spectra from (non-polarizable) FF-MD simulations in Fig. 3(c) (inset blue and red lines) and the core-charge autocorrelation spectra in Fig. 6(a) also show a broad response in the low THz regime, indicating that the band broadening is caused by molecular rotations and not by electronic effects.

In the 1–30 THz region, the bulk water spectrum has two main features at 20 and 5 THz, attributed to hindered rotations (librations) and hydrogen-bond stretch vibrations, respectively. These can be described based on the power spectrum of two observables based on atomic core positions:[46] the power spectrum,

$$\tilde{S}_{\mathbf{\Omega}}(\omega) = \int_{-\infty}^{\infty} \mathrm{d}t\, \langle \mathbf{\Omega}(0) \cdot \mathbf{\Omega}(t) \rangle e^{i\omega t}, \tag{24}$$

of the angular velocity of the water molecule bisector $\mathbf{\Omega}$ [see Fig. 6(i)], indicated by the dashed lines shown in Figs. 6(f) and 6(g), which qualitatively reproduces the libration peak, and the power spectrum,

$$\tilde{S}_{d_{\mathrm{OO}}} = \int_{-\infty}^{\infty} \mathrm{d}t\, \langle d_{\mathrm{OO}}(0) d_{\mathrm{OO}}(t) \rangle e^{i\omega t}, \tag{25}$$

of the oxygen–oxygen distance of hydrogen-bonded water pairs d_{OO} [see Fig. 6(i)] indicated by the dotted lines shown in Figs. 6(f) and 6(g), which reproduces the hydrogen-bond stretch peak at 5 THz. In Figs. 6(f) and 6(g), we further decompose these power spectra into parallel and perpendicular components. The peak of $\tilde{S}_{d_{\mathrm{OO}}}$ is only shifted marginally in frequency when going from bulk (black dotted line) to confinement (red dotted line), while its intensity changes. The increase in intensity of $\tilde{S}^{\parallel}_{d_{\mathrm{OO}}}$ and the simultaneous vanishing intensity of $S^{\perp}_{d_{\mathrm{OO}}}$ in nanoconfinement can be attributed to an average orientation of hydrogen-bonds parallel to the graphene (see the supplementary material, Sec. S8 for more details on $\tilde{S}^{\perp}_{d_{\mathrm{OO}}}$ and $\tilde{S}^{\parallel}_{d_{\mathrm{OO}}}$).

The rotational power spectrum $\tilde{S}_{\mathbf{\Omega}}$ on the other hand changes from a band localized between 10 and 30 in bulk [black dashed line in Figs. 6(f) and 6(g)] to a band spanning the entire range from 1 to 30 THz in confinement (red dashed line), similar to the effective susceptibility. This shows that the emergence of the broad absorption band in confinement is indeed caused by single-molecule rotation. This can be linked to a change of the hydrogen bonding pattern, which has been reported in nanoconfined water.[57] In particular, it has been shown that the geometric arrangement of water molecules transitions from tetrahedral in bulk to different lattice structures in single layer nanoconfinement, depending on the temperature and the pressure.[60] A representative molecular structure of our $L = 0.7$ nm system is shown in Fig. 6(h), together with the orientational ordering of water as quantified by the spatial dipole correlation function $\langle \mu_i^{\parallel}(0) \mu_j^{\parallel}(r) \rangle / \langle \mu_i^{\parallel} \rangle^2$, where $\mu_i^{\parallel}$ denotes the component of the dipole moment of molecule i parallel to graphene. In bulk water (black line), the orientational correlation decays rapidly over the first two hydration shells of a water molecule, while in the $L = 0.7$ nm system (red line) as well as in interfacial water of the $L = 3.4$ nm system (cyan line), it decays over about five hydration layers. This high spatial ordering results in a delocalization of the libration mode, so that water molecules of the second hydration shell also participate to the libration. By performing time-frequency analysis (see Sec. S9 of the supplementary material), we determine the spatial range of this libration correlation. In bulk water, we find that the libration of water molecules is correlated up to a distance of around 3.5 Å, i.e., only neighboring water molecules librate in a synchronized fashion, which reflects the two-body nature of the libration motion.[46] However, in $L = 0.7$ nm confinement, the librational motion of different water molecules is correlated over distances of up to 6 Å. This indicates that there is a transition from a two-body to a multi-body vibration characterized by many distinct normal modes, which causes the broad libration band between 1 and 30 THz in confined water. Interestingly, also the first hydration layer of the $L = 3.4$ nm system [Fig. 6(h) cyan line] shows long-ranged orientational organization. Due to this, a broadening of the libration peak can be seen to a lesser degree also in the $L = 1.4$ and $L = 3.4$ nm systems [Figs. 6(d) and 6(e) green and orange lines].

III. CONCLUSION

We extract the frequency-dependent anisotropic electric susceptibility of nanoconfined water from FF-MD and DFT-MD simulations and introduce a box model for the polarization response to applied $\tilde{E}_{\parallel}(\omega)$ and $\tilde{D}_{\perp}(\omega)$ fields. We find that the derived effective susceptibility, which is typically reported in experiments, is strongly sensitive to the effective box length, in the perpendicular direction at low frequencies. Moreover, we show that the polarizability of the confining surfaces influences the effective susceptibility. In the case of experimental suspended graphene, frequency independent absorption has been experimentally observed, which is attributed to electronic interband-transitions[61,62] not included in DFT-MD simulations. Adding the imaginary part to the electronic polarizability $a_{\parallel/\perp}$ in our model would alter the effective susceptibility even further.

The sensitivity of the effective susceptibilities to the effective length L^{eff} is rationalized by decomposing the response into bulk and excess contributions. The excess function can be further decomposed into a confinement-length-independent interface excess and a confinement excess, which allows for the quantification of the influence of geometric confinement vs interfacial effects on the frequency-dependent susceptibility. In the case of water confined between two graphene surfaces, confinement effects are absent for confinement lengths $L \geq 1.4$ nm, i.e., above a confinement length

of a nanometer, the spectra can be explained by the sum of bulk water and interface contributions. The onset of confinement effects at around $L = 1$ nm is largely independent of frequency.

By analyzing FF-MD simulations of water confined between graphene sheets at different confinement lengths and extracting surface and confinement excess spectra, we show that the Debye relaxation at 15 GHz of water parallel to the interface is enhanced due to stronger orientational correlation of interfacial water. At the same time, collective rotations are slowed down at the interface leading to a redshift of the Debye peak. Employing DFT-MD simulations, we recover experimentally reported changes in the intramolecular dynamics of water at interfaces, in particular a blue shift of the OH stretch vibration, which we explain with an increased curvature of the effective OH bond potential. Strikingly, the HOH bend peak shows the opposite behavior and undergoes a red shift. The slow-down of the Debye relaxation, the red shift of the HOH bend, and the blue shift of the OH stretch vibration are all predominantly interfacial effects with only small additional effects due to geometric confinement.

Below the confinement threshold, the arrangement of water changes and we find significant confinement effects, most prominently in the spectral range from 1 to 30 THz. In bulk water, two distinct peaks at 5 and 20 THz caused by hydrogen-bond stretching and hindered molecular rotations are found. In two-dimensional water layers, however, a broad spectral band, ranging over the entire spectral range from 1 to 30 THz, appears due to collective molecular rotation. Compared to bulk, the libration band in confinement is not only considerably broader but also redshifted to nearly half its usual frequency. We relate this to a transition of the libration motion from a two-body mode in bulk to a delocalized multibody mode in nanoconfinement. While there are some signs of similar motion also in the first hydration layer of water at graphene surfaces, reflecting its two-dimensional nature, the described broad rotational band is largely confinement-induced and a striking signature of geometrically confined water.

IV. METHODS

A. FF-MD simulations

FF-MD simulations are performed using GROMACS 2021[63] with the SPC/E water model and GROMOS 53A6[64] parameters for carbon atoms. Simulations are performed in the NVT ensemble using the canonical sampling through velocity rescaling (CSVR)[65] thermostat at 300 K. We use a 2 fs time step and truncate Lennard-Jones interactions at 0.9 nm. Treatment of electrostatic interactions employs a real-space cutoff at 0.9 nm, while long-range interactions are handled with the particle mesh Ewald method.[66] During the simulation, all carbon atoms remain frozen. To cover the full range of frequencies, we conduct multiple MD simulations at different lengths and write-out frequencies. For each confinement length, we conduct a 2 μs and at least ten times 10 ns simulations for which we write out atomic positions every 400 and 2 fs, respectively. We calculate polarization-autocorrelation functions for each system and assemble the full correlation function in the time domain from the first 1600 fs of the 10 ns trajectories and the rest from the 2 μs trajectory. Correlation functions from shorter simulations are shifted additively by a constant to match the 2 μs correlation function at $t = 0$ to give smooth correlation functions. The assembled correlation function is truncated when it first takes a negative value and a one-sided Fourier transform is calculated numerically with a trapezoidal integration rule. Bulk water simulations have been performed with 1410 water molecules in a $(3.5\ \text{nm})^3$ box for 100 ns. All the presented FF-MD spectra are smoothed in logarithmic frequency space with a Gaussian kernel. This corresponds to smoothing with a kernel with varying width, corresponding to 3% of the kernel's center frequency.

To determine spatially resolved dielectric profiles according to Eqs. (7)–(10) from FF-MD simulations, parallel and perpendicular polarization density profiles are extracted. The perpendicular polarization density is determined by taking into account the instantaneous charge density profile,

$$\rho_Z(\mathbf{r}, t) = \sum_i Z_i \delta(\mathbf{q} - \mathbf{r}_i(t)), \tag{26}$$

where we sum over all atoms with positions $\mathbf{q}_i(t)$ and partial charges Z_i. The perpendicular polarization density, assuming no external electric field is applied, is found by integration, using

$$m_\perp(z, t) = -\int_0^z \mathrm{d}z\, \rho_Z(z', t). \tag{27}$$

Parallel polarization densities are obtained using the virtual cutting method introduced by Bonthuis *et al.*[47]

B. DFT-MD simulations

DFT-MD simulations are carried out with CP2K 7.1 software[67] within the Born–Oppenheimer approximation. We use the BLYP[68,69] exchange–correlation functional with Grimme-D3[70] dispersion correction, GTH pseudopotentials[71] and combine it with the DZVP-SR-MOLOPT basis set.[72] The plane wave expansion of the electronic density is truncated at 400 Ry. DFT-MD simulations are conducted with a time step of 0.5 fs. As in FF-MD simulations, carbon atoms are frozen during all simulations. Each system is first equilibrated in FF-MD for 1 ns and subsequently for 5 ps in DFT-MD. Production runs are performed for at least 75 ps each using the CSVR thermostat at 300 K. Total system dipole moments are calculated according to the implementation in CP2K. The total polarization is determined modulo a period so that it depends on the lattice vectors. We reconstruct a continuous polarization trajectory by assuming polarization changes between successive MD steps to be smaller than half of that period. The imaginary part of the dielectric spectra is extracted by using the Wiener–Khintschin theorem on the polarization trajectories $M(t)$,

$$\chi''_{\alpha\beta}(\omega) = \frac{\omega}{\varepsilon_0 k_\mathrm{B} T L_t} \tilde{M}_\alpha(\omega) \tilde{M}^*_\beta(\omega), \tag{28}$$

with total simulation time L_t. Real parts are then calculated numerically with the Kramers–Kronig relation, according to[73]

$$\chi'_{\alpha\beta}(\omega) = -\mathcal{F}^{-1}\left[i\ \mathrm{sgn}(t)\, \mathcal{F}[\chi''_{\alpha\beta}(\omega)](t)\right], \tag{29}$$

with the Fourier-transform $\mathcal{F}[f](\omega) = \tilde{f}(\omega)$ as defined in the main text and its inverse $\mathcal{F}^{-1}$. All spectra are smoothed with a Gaussian kernel in the frequency domain at constant width of 0.4 THz. Bulk water simulations have been taken from Ref. 46.

C. Electronic polarizabilities

As shown in the supplementary material, Sec. S2, the polarization density at given atomic core positions q is an explicit function of the applied external field if the system is instantaneously polarizable. The electronic polarizability is defined by

$$a_{\alpha\beta}(z) = \left\langle \frac{\partial}{\partial E^{\mathrm{ext}}_{\beta}} m_{\alpha}(z, q, \mathbf{E}^{\mathrm{ext}}_{\mathrm{post}}) \Big|_{\mathbf{E}^{\mathrm{ext}}_{\mathrm{post}}=\mathbf{0}} \right\rangle_{\mathbf{E}^{\mathrm{ext}}_{\mathrm{traj}}=\mathbf{0}}. \tag{30}$$

Here, $\langle\cdot\rangle_{\mathbf{E}^{\mathrm{ext}}_{\mathrm{traj}}=\mathbf{0}}$ denotes an average over a core-position trajectory that is simulated without applying an external field, while $m_{\alpha}(z, q, \mathbf{E}^{\mathrm{ext}}_{\mathrm{post}})$ denotes the (post-processed) calculation of the polarization density with applied external field $\mathbf{E}^{\mathrm{ext}}_{\mathrm{post}}$. In case of a system that is uniform in x and y directions, the electronic polarizability is a diagonal tensor with two independent components $a_{\parallel} = a_{xx} = a_{yy}$ and $a_{\perp} = a_{zz}$. From our unperturbed (zero-field) DFT-MD simulations, we take snapshots every 500 fs and determine the polarization of the system in post-processing at fixed nuclei positions for each frame with and without an externally applied field of nominally $\hat{E}^{\mathrm{ext}} = 0.512$ V/nm. The polarizability is calculated from a finite difference scheme, according to

$$a_{\alpha\beta}(z) = \frac{\left\langle m_{\alpha}(z, q, \mathbf{e}_{\beta}\hat{E}^{\mathrm{ext}})\right\rangle_{\mathbf{0}} - \langle m_{\alpha}(z, q, \mathbf{0})\rangle_{\mathbf{0}}}{\hat{E}^{\mathrm{ext}}}, \tag{31}$$

where $\mathbf{e}_{\beta}$ denotes the unit vector in the β direction. The graphene sheet polarizability $A^{\mathrm{graph}}_{\perp} = \int_V \mathrm{d}\mathbf{r}\, a^{\mathrm{graph}}_{\perp}(z)$ is calculated accordingly for the separations $L = 0.7$ nm, $L = 1.4$ nm, and $L = 3.4$ nm from single-energy calculations of the graphene sheets without water in between.

SUPPLEMENTARY MATERIAL

The supplementary material contains derivations of the Green–Kubo relations in Eqs. (7) and (8), the box model in Eqs. (11) and (12), and the Green–Kubo relation in Eq. (22). It contains further details on the relation between spectroscopic experiments and effective susceptibilities, time-frequency analysis of the libration feature that allows for the interpretation of spectra shown in Figs. 6(d) and 6(e), fit parameters of HOH bend and OH stretch peaks, and additional remarks on effective susceptibilities helpful for the understanding of this work.

ACKNOWLEDGMENTS

We acknowledge the support by Deutsche Forschungsgemeinschaft under Grant No. CRC 1349, code 387284271, Project C04. Computational resources were provided from Hochleistungsrechenzentrum Norddeutschland under Project No. bep00106, as well as the HPC clusters at the physics department and ZEDAT, FU Berlin. We further thank Laura Scalfi and Louis Lehmann for fruitful discussions.

AUTHOR DECLARATIONS

Conflict of Interest

The authors have no conflicts to disclose.

Author Contributions

Maximilian R. Becker: Conceptualization (equal); Investigation (equal); Methodology (equal); Software (equal); Visualization (equal); Writing – original draft (equal). **Roland R. Netz**: Conceptualization (equal); Funding acquisition (equal); Investigation (equal); Methodology (equal); Supervision (equal); Writing – original draft (equal).

DATA AVAILABILITY

The data that support the findings of this study are available from the corresponding author upon reasonable request.

REFERENCES

[1] U. Raviv, P. Laurat, and J. Klein, "Fluidity of water confined to subnanometre films," Nature **413**, 51–54 (2001).
[2] J. C. Rasaiah, S. Garde, and G. Hummer, "Water in nonpolar confinement: From nanotubes to proteins and beyond," Annu. Rev. Phys. Chem. **59**, 713–740 (2008).
[3] S. Jähnert, F. Vaca Chávez, G. E. Schaumann, A. Schreiber, M. Schönhoff, and G. H. Findenegg, "Melting and freezing of water in cylindrical silica nanopores," Phys. Chem. Chem. Phys. **10**, 6039–6051 (2008).
[4] E. Secchi, S. Marbach, A. Niguès, D. Stein, A. Siria, and L. Bocquet, "Massive radius-dependent flow slippage in carbon nanotubes," Nature **537**, 210–213 (2016).
[5] D. Munoz-Santiburcio and D. Marx, "Confinement-controlled aqueous chemistry within nanometric slit pores: Focus review," Chem. Rev. **121**, 6293–6320 (2021).
[6] J. B. Brubach, A. Mermet, A. Filabozzi, A. Gerschel, D. Lairez, M. P. Krafft, and P. Roy, "Dependence of water dynamics upon confinement size," J. Phys. Chem. B **105**, 430–435 (2001).
[7] S. Le Caër, S. Pin, S. Esnouf, Q. Raffy, J. P. Renault, J. B. Brubach, G. Creff, and P. Roy, "A trapped water network in nanoporous material: The role of interfaces," Phys. Chem. Chem. Phys. **13**, 17658–17666 (2011).
[8] M. Baum, F. Rieutord, F. Juranyi, C. Rey, and D. Rébiscoul, "Dynamical and structural properties of water in silica nanoconfinement: Impact of pore size, ion nature, and electrolyte concentration," Langmuir **35**, 10780–10794 (2019).
[9] X. Xu, X. Jin, M. Kuehne, D.-L. Bao, J. Martis, Y.-M. Tu, C. L. Ritt, J. C. Idrobo, M. S. Strano, A. Majumdar *et al.*, "Hydrogen bonding in water under extreme confinement unveiled by nanoscale vibrational spectroscopy and simulations," arXiv:2402.17989 (2024).
[10] A. Scodinu and J. T. Fourkas, "Comparison of the orientational dynamics of water confined in hydrophobic and hydrophilic nanopores," J. Phys. Chem. B **106**, 10292–10295 (2002).
[11] A. Taschin, P. Bartolini, A. Marcelli, R. Righini, and R. Torre, "A comparative study on bulk and nanoconfined water by time-resolved optical kerr effect spectroscopy," Faraday Discuss. **167**, 293–308 (2013).
[12] A. M. Dokter, S. Woutersen, and H. J. Bakker, "Anomalous slowing down of the vibrational relaxation of liquid water upon nanoscale confinement," Phys. Rev. Lett. **94**, 178301 (2005).
[13] D. E. Moilanen, N. E. Levinger, D. B. Spry, and M. D. Fayer, "Confinement or the nature of the interface? Dynamics of nanoscopic water," J. Am. Chem. Soc. **129**, 14311–14318 (2007).

[14]S. A. Yamada, J. Y. Shin, W. H. Thompson, and M. D. Fayer, "Water dynamics in nanoporous silica: Ultrafast vibrational spectroscopy and molecular dynamics simulations," J. Phys. Chem. C **123**, 5790–5803 (2019).
[15]R. Musat, J. P. Renault, M. Candelaresi, D. J. Palmer, S. LeCaër, R. Righini, and S. Pommeret, "Finite size effects on hydrogen bonds in confined water," Angew. Chem., Int. Ed. **47**, 8033–8035 (2008).
[16]A. W. Knight, N. G. Kalugin, E. Coker, and A. G. Ilgen, "Water properties under nano-scale confinement," Sci. Rep. **9**, 8246 (2019).
[17]A. A. Bakulin, D. Cringus, P. A. Pieniazek, J. L. Skinner, T. L. Jansen, and M. S. Pshenichnikov, "Dynamics of water confined in reversed micelles: Multidimensional vibrational spectroscopy study," J. Phys. Chem. B **117**, 15545–15558 (2013).
[18]T. Yamaguchi, H. Furuhashi, T. Matsuoka, and S. Koda, "Dynamic solvophobic effect and its cooperativity in the hydrogen-bonding liquids studied by dielectric and nuclear magnetic resonance relaxation," J. Phys. Chem. B **112**, 16633–16641 (2008).
[19]D. Laage, G. Stirnemann, and J. T. Hynes, "Why water reorientation slows without iceberg formation around hydrophobic solutes," J. Phys. Chem. B **113**, 2428–2435 (2009).
[20]I. R. Piletic, D. E. Moilanen, D. B. Spry, N. E. Levinger, and M. D. Fayer, "Erratum: Testing the core/shell model of nanoconfined water in reverse micelles using linear and nonlinear IR spectroscopy [J. Phys. Chem. A **110A**, 4985 (2006)]," J. Phys. Chem. A **110**, 10369 (2006).
[21]W. H. Thompson, "Perspective: Dynamics of confined liquids," J. Chem. Phys. **149**, 170901 (2018).
[22]D. J. Bonthuis, S. Gekle, and R. R. Netz, "Dielectric profile of interfacial water and its effect on double-layer capacitance," Phys. Rev. Lett. **107**, 166102–166105 (2011).
[23]O. Björneholm, M. H. Hansen, A. Hodgson, L.-M. Liu, D. T. Limmer, A. Michaelides, P. Pedevilla, J. Rossmeisl, H. Shen, G. Tocci *et al.*, "Water at interfaces," Chem. Rev. **116**, 7698–7726 (2016).
[24]G. Gonella, E. H. Backus, Y. Nagata, D. J. Bonthuis, P. Loche, A. Schlaich, R. R. Netz, A. Kühnle, I. T. McCrum, M. T. Koper, M. Wolf, B. Winter, G. Meijer, R. K. Campen, and M. Bonn, "Water at charged interfaces," Nat. Rev. Chem. **5**, 466 (2021).
[25]N. Dupertuis, O. B. Tarun, C. Lütgebaucks, and S. Roke, "Three-dimensional confinement of water: H_2O exhibits long-range (>50 nm) structure while D_2O does not," Nano Lett. **22**, 7394–7400 (2022).
[26]Y. Wang, F. Tang, X. Yu, K.-Y. Chiang, C.-C. Yu, T. Ohto, Y. Chen, Y. Nagata, and M. Bonn, "Interfaces govern structure of angstrom-scale confined water," arXiv:2310.10354 (2023).
[27]P. A. Pieniazek, Y. S. Lin, J. Chowdhary, B. M. Ladanyi, and J. L. Skinner, "Vibrational spectroscopy and dynamics of water confined inside reverse micelles," J. Phys. Chem. B **113**, 15017–15028 (2009).
[28]S. Gekle and R. R. Netz, "Anisotropy in the dielectric spectrum of hydration water and its relation to water dynamics," J. Chem. Phys. **137**, 104704 (2012).
[29]A. Schlaich, E. W. Knapp, and R. R. Netz, "Water dielectric effects in planar confinement," Phys. Rev. Lett. **117**, 048001 (2016).
[30]S. Ruiz-Barragan, F. Sebastiani, P. Schienbein, J. Abraham, G. Schwaab, R. R. Nair, M. Havenith, and D. Marx, "Nanoconfinement effects on water in narrow graphene-based slit pores as revealed by THz spectroscopy," Phys. Chem. Chem. Phys. **24**, 24734–24747 (2022).
[31]M. F. Calegari Andrade and T. A. Pham, "Probing confinement effects on the infrared spectra of water with deep potential molecular dynamics simulations," J. Phys. Chem. Lett. **14**, 5560–5566 (2023).
[32]B. Das, S. Ruiz-Barragan, and D. Marx, "Deciphering the properties of nanoconfined aqueous solutions by vibrational sum frequency generation spectroscopy," J. Phys. Chem. Lett. **14**, 1208–1213 (2023).
[33]B. Coquinot, M. Becker, R. R. Netz, L. Bocquet, and N. Kavokine, "Collective modes and quantum effects in two-dimensional nanofluidic channels," Faraday Discuss. **249**, 162–180 (2024).
[34]L. Fumagalli, A. Esfandiar, R. Fabregas, S. Hu, P. Ares, A. Janardanan, Q. Yang, B. Radha, T. Taniguchi, K. Watanabe, G. Gomila, K. S. Novoselov, and A. K. Geim, "Anomalously low dielectric constant of confined water," Science **360**, 1339–1342 (2018).
[35]C. Zhang, "Note: On the dielectric constant of nanoconfined water," J. Chem. Phys. **148**, 1802–02030 (2018).
[36]S. Ruiz-Barragan, D. Muñoz-Santiburcio, S. Körning, and D. Marx, "Quantifying anisotropic dielectric response properties of nanoconfined water within graphene slit pores," Phys. Chem. Chem. Phys. **22**, 10833–10837 (2020).
[37]P. Loche, C. Ayaz, A. Wolde-Kidan, A. Schlaich, and R. R. Netz, "Universal and nonuniversal aspects of electrostatics in aqueous nanoconfinement," J. Phys. Chem. B **124**, 4365–4371 (2020).
[38]F. Deißenbeck, C. Freysoldt, M. Todorova, J. Neugebauer, and S. Wippermann, "Dielectric properties of nanoconfined water: A canonical thermopotentiostat approach," Phys. Rev. Lett. **126**, 136803 (2021).
[39]T. Dufils, C. Schran, J. Chen, A. K. Geim, L. Fumagalli, and A. Michaelides, "Origin of dielectric polarization suppression in confined water from first principles," Chem. Sci. **15**, 516–527 (2024).
[40]M. Becker, P. Loche, M. Rezaei, A. Wolde-Kidan, Y. Uematsu, R. Netz, and D. Bonthuis, "Multiscale modeling of aqueous electric double layers," Chem. Rev. **124**, 1–26 (2023).
[41]Y. Rezus and H. Bakker, "Strong slowing down of water reorientation in mixtures of water and tetramethylurea," J. Phys. Chem. A **112**, 2355–2361 (2008).
[42]K.-J. Tielrooij, J. Hunger, R. Buchner, M. Bonn, and H. J. Bakker, "Influence of concentration and temperature on the dynamics of water in the hydrophobic hydration shell of tetramethylurea," J. Am. Chem. Soc. **132**, 15671–15678 (2010).
[43]H. J. Berendsen, J. R. Grigera, and T. P. Straatsma, "The missing term in effective pair potentials," J. Phys. Chem. **91**, 6269–6271 (1987).
[44]H. A. Stern and S. E. Feller, "Calculation of the dielectric permittivity profile for a nonuniform system: Application to a lipid bilayer simulation," J. Chem. Phys. **118**, 3401–3412 (2003).
[45]S. Gekle and R. R. Netz, "Nanometer-resolved radio-frequency absorption and heating in biomembrane hydration layers," J. Phys. Chem. B **118**, 4963–4969 (2014).
[46]S. Carlson, F. N. Brünig, P. Loche, D. J. Bonthuis, and R. R. Netz, "Exploring the absorption spectrum of simulated water from MHz to infrared," J. Phys. Chem. A **124**, 5599–5605 (2020).
[47]D. J. Bonthuis, S. Gekle, and R. R. Netz, "Profile of the static permittivity tensor of water at interfaces: Consequences for capacitance, hydration interaction and ion adsorption," Langmuir **28**, 7679–7694 (2012).
[48]A. Kornyshev, S. Leikin, and G. Sutmann, "'Overscreening' in a polar liquid as a result of coupling between polarization and density fluctuations," Electrochim. Acta **42**, 849–865 (1997), part of Special Issue: Fundamental Aspects of Electrochemistry.
[49]M. R. Becker, P. Loche, D. J. Bonthuis, D. Mouhanna, R. R. Netz, and H. Berthoumieux, "Dielectric properties of aqueous electrolytes at the nanoscale," arXiv:2303.14846 (2023).
[50]P. Loche, A. Wolde-Kidan, A. Schlaich, D. J. Bonthuis, and R. R. Netz, "Comment on 'Hydrophobic surface enhances electrostatic interaction in water'," Phys. Rev. Lett. **123**, 049601 (2019).
[51]J. Hasted, S. Husain, F. Frescura, and J. Birch, "Far-infrared absorption in liquid water," Chem. Phys. Lett. **118**, 622–625 (1985).
[52]C. Fecko, J. Eaves, J. Loparo, A. Tokmakoff, and P. Geissler, "Ultrafast hydrogen-bond dynamics in the infrared spectroscopy of water," Science **301**, 1698–1702 (2003).
[53]M. Heyden, J. Sun, S. Funkner, G. Mathias, H. Forbert, M. Havenith, and D. Marx, "Dissecting the THz spectrum of liquid water from first principles via correlations in time and space," Proc. Natl. Acad. Sci. U. S. A. **107**, 12068–12073 (2010).
[54]Q. Du, R. Superfine, E. Freysz, and Y. Shen, "Vibrational spectroscopy of water at the vapor/water interface," Phys. Rev. Lett. **70**, 2313 (1993).
[55]L. Scatena, M. Brown, and G. Richmond, "Water at hydrophobic surfaces: Weak hydrogen bonding and strong orientation effects," Science **292**, 908–912 (2001).
[56]C.-S. Hsieh, R. K. Campen, A. C. Vila Verde, P. Bolhuis, H.-K. Nienhuys, and M. Bonn, "Ultrafast reorientation of dangling OH groups at the air-water interface using femtosecond vibrational spectroscopy," Phys. Rev. Lett. **107**, 116102 (2011).
[57]S. Ruiz-Barragan, D. Munoz-Santiburcio, and D. Marx, "Nanoconfined water within graphene slit pores adopts distinct confinement-dependent regimes," J. Phys. Chem. Lett. **10**, 329–334 (2018).

[58]M. R. Becker, P. Loche, and R. R. Netz, "Electrokinetic, electrochemical, and electrostatic surface potentials of the pristine water liquid-vapor interface," J. Chem. Phys. **157**, 240902 (2022).
[59]F. N. Brünig, O. Geburtig, A. v. Canal, J. Kappler, and R. R. Netz, "Time-dependent friction effects on vibrational infrared frequencies and line shapes of liquid water," J. Phys. Chem. B **126**, 1579–1589 (2022).
[60]V. Kapil, C. Schran, A. Zen, J. Chen, C. J. Pickard, and A. Michaelides, "The first-principles phase diagram of monolayer nanoconfined water," Nature **609**, 512–516 (2022).
[61]R. R. Nair, P. Blake, A. N. Grigorenko, K. S. Novoselov, T. J. Booth, T. Stauber, N. M. Peres, and A. K. Geim, "Fine structure constant defines visual transparency of graphene," Science **320**, 1308 (2008).
[62]K. F. Mak, M. Y. Sfeir, Y. Wu, C. H. Lui, J. A. Misewich, and T. F. Heinz, "Measurement of the optical conductivity of graphene," Phys. Rev. Lett. **101**, 196405 (2008).
[63]M. J. Abraham, T. Murtola, R. Schulz, S. Páll, J. C. Smith, B. Hess, and E. Lindahl, "GROMACS: High performance molecular simulations through multi-level parallelism from laptops to supercomputers," SoftwareX **1–2**, 19–25 (2015).
[64]C. Oostenbrink, A. Villa, A. E. Mark, and W. F. Van Gunsteren, "A biomolecular force field based on the free enthalpy of hydration and solvation: The GROMOS force-field parameter sets 53A5 and 53A6," J. Comput. Chem. **25**, 1656–1676 (2004).
[65]G. Bussi, D. Donadio, and M. Parrinello, "Canonical sampling through velocity rescaling," J. Chem. Phys. **126**, 014101 (2007).
[66]U. Essmann, L. Perera, M. L. Berkowitz, T. Darden, H. Lee, and L. G. Pedersen, "A smooth particle mesh Ewald method," J. Chem. Phys. **103**, 8577–8593 (1995).
[67]T. D. Kühne, M. Iannuzzi, M. Del Ben, V. V. Rybkin, P. Seewald, F. Stein, T. Laino, R. Z. Khaliullin, O. Schütt, F. Schiffmann, *et al.*, "CP2K: An electronic structure and molecular dynamics software package-quickstep: Efficient and accurate electronic structure calculations," J. Chem. Phys. **152**, 194103 (2020).
[68]A. D. Becke, "Density-functional exchange-energy approximation with correct asymptotic behavior," Phys. Rev. A **38**, 3098–3100 (1988).
[69]C. Lee, W. Yang, and R. G. Parr, "Development of the Colle-Salvetti correlation-energy formula into a functional of the electron density," Phys. Rev. B **37**, 785–789 (1988).
[70]S. Grimme, J. Antony, S. Ehrlich, and H. Krieg, "A consistent and accurate *ab initio* parametrization of density functional dispersion correction (DFT-D) for the 94 elements H-Pu," J. Chem. Phys. **132**, 154104 (2010).
[71]S. Goedecker, M. Teter, and J. Hutter, "Separable dual-space Gaussian pseudopotentials," Phys. Rev. B **54**, 1703–1710 (1996).
[72]J. VandeVondele and J. Hutter, "Gaussian basis sets for accurate calculations on molecular systems in gas and condensed phases," J. Chem. Phys. **127**, 114105 (2007).
[73]J. Lucas, E. Géron, T. Ditchi, and S. Holé, "A fast Fourier transform implementation of the Kramers-Kronig relations: Application to anomalous and left handed propagation," AIP Adv. **2**, 032144 (2012).